Check for updates

ADVANCED OPTICAL MATERIALS
www.advopticalmat.de

Highly Efficient Photoanodic Material: Utilizing Dihydrolipoic Acid-Functionalized $CuInS_2$ Quantum Dots in Photoelectrochemical Cells

*Giacomo Morselli, Caterina Bellatreccia, Michele Mazzanti, Vito Cristino, Anna Ianniello, Stefano Caramori, Raffaello Mazzaro, and Paola Ceroni**

Copper indium sulfide quantum dots (CIS QDs) possess the desired optical properties to act as photoanodic material in photoelectrochemical cells, like a high molar absorption coefficient over the entire visible spectrum and long exciton lifetimes. The already reported procedures that utilize photoanodes based on such nanoparticles, however, exploit harsh conditions or utilize non-scalable, expensive, and low-yield syntheses. Here, the construction of CIS QDs adsorbed onto TiO_2/FTO photoanodes (FTO = fluorine-doped tin oxide) with a process aimed at avoiding these issues is proposed. In particular, the employment of dihydrolipoic acid as the ligand allows an easy and cost-effective functionalization. CdS layers are deposited onto the nanoparticles to enhance the photoelectrochemical properties. Full characterization of the steady–state and transient photoelectrochemical properties of the electrodes is performed to gain information on the interfacial dynamics among the different components of the electrode. Maximum IPCEs of the order of 50% and a spectral sensitization extended up to 700 nm are obtained in the optimized conditions.

1. Introduction

In the last two decades, semiconducting nanoparticles, or quantum dots (QDs), have been studied as a replacement for molecular sensitizers in photoanodes for dye-sensitized solar cells (DSSCs) and photoelectrochemical cells (PECs).[1–3] The main advantages are related to their bandgap tunability, elevated absorption in the visible spectral range, high photostability, and the possibility of multiple excitons generation.[4]

Among them, ternary $CuInS_2$ quantum dots (CIS QDs) possess desirable characteristics to act as photosensitizers: i) low toxicity and cost-effectiveness, ii) tunability of the bandgap according to the stoichiometry and dimension, iii) high molar absorption coefficients over the entire visible spectral range (10^4–10^5 M^{-1} cm^{-1}), and iv) long emission lifetimes (tens to hundred nanoseconds) that can be exploited for charge separation applications.[5–8]

CIS QDs have been coupled to TiO_2 electrodes thanks to the relative position of the bands.[9–12] Their conduction band lays at superior energies if compared to the TiO_2 one,[13] therefore, charge separation can occur upon irradiation of CIS QDs: the electron promoted from the valence to the conduction band of the ternary nanoparticle leaps to the conduction band of titanium dioxide. A positive hole remains localized in the valence band of CIS, which can be exploited to perform oxidation reactions.[14,15]

To ameliorate the efficiency of the CIS QDs-based photoanode and to suppress the losses caused by surface defects, a CdS layer has been deposited to form a "quasi-type II" structure. This has

G. Morselli[+], C. Bellatreccia, P. Ceroni
Department of Chemistry "G. Ciamician"
University of Bologna
via Selmi 2, Bologna 40126, Italy
E-mail: paola.ceroni@unibo.it

The ORCID identification number(s) for the author(s) of this article can be found under https://doi.org/10.1002/adom.202400259

[+]Present address: Department of Chemistry, University of Basel, St. Johanns-Ring 19, 4056 Basel, Switzerland

© 2024 The Author(s). Advanced Optical Materials published by Wiley-VCH GmbH. This is an open access article under the terms of the Creative Commons Attribution-NonCommercial License, which permits use, distribution and reproduction in any medium, provided the original work is properly cited and is not used for commercial purposes.

[Correction added on September 18, 2024, after online publication: The copyright line has been corrected in this version.]

DOI: 10.1002/adom.202400259

M. Mazzanti, V. Cristino, A. Ianniello, S. Caramori
Department of Chemical
Pharmaceutical and Agricultural Sciences
University of Ferrara
via Borsari 46, Ferrara 44121, Italy

R. Mazzaro
Department of Physics and Astronomy
University of Bologna
viale Berti Pichat 6/2, Bologna 40127, Italy

R. Mazzaro
Institute for Microelectronics and Microsystems
National Research Council
via Gobetti 101, Bologna 40129, Italy

 © 2024 The Author(s). Advanced Optical Materials published by Wiley-VCH GmbH

Table 1. State of art of the methods used for the realization of CIS-QDs-based photoanodes and their relative performances. All measurements are performed in SO_3^{2-}/S^{2-} or S^{2-} electrolyte.

Junction scheme	Synthetic method	Deposition method	Peak photo-current density/mA cm^{-2}	IPCE (500 nm)/%	Reference
$CuInS_2/TiO_2$	Hot-injection	Self-assembly with mercaptopropionic acid	3.6	n.a.	T.L. Li et al.[17]
$CuInS_2/CdS/TiO_2$	Heating-up	Electrophoretic deposition at 200 V	6	45	C. Wang et al.[18]
$CuInS_2/TiO_2$	Thermolysis	Electrophoretic deposition at 60 V	n.a.	45	Z. Peng et al.[19]
$CuInS_2/TiO_2$	Pulsed laser deposition in high vacuum. Annealing temperature: 500 °C	Pulsed laser deposition	n.a.	42	M. Han et al.[20]
$CuInS_2/In_2S_3/TiO_2$	Heating-up	Self-assembly with dodecanethiol and thermal treatment at 350 °C	2.4	30	Y. Chen et al.[21]
$CuInS_2/CdS/TiO_2$	Aqueous	Self-assembly with mercaptoacetic acid	n.a.	45	X. Hu *et.al.*[22]
$Mn\text{-}CuInS_2/ZnS/TiO_2$	Hot-injection	Electrophoretic deposition at 100 V	6	n.a.	R. Wang et al.[23]
$CuInSe_eS_{2-x}$	Heating-up	Electrophoretic deposition at 200 V	5	n.a.	X. Tong et al.[3]
$CuInS_2/CdS/TiO_2$	Heating-up	Self-assembly with dihydrolipoic acid	6.5	52	This work

been deposited either by epitaxial growth on CIS QDs during the synthesis process,[16] or by SILAR (successive ionic layer adsorption and reaction) method.[17,18]

Table 1 summarizes previous studies on CIS QDs-based photoelectrochemical cells, with their relative performance in terms of incident photon to current efficiency (IPCE) and photocurrents. The main drawbacks of CIS QDs-based photoanodes reported so far are related to the synthesis of the nanoparticles, by hot-injection technique or an aqueous approach that is not able to produce high-quality nanoparticles with a good yield.[9,11,12,19] An alternative synthetic route proposed in 2011 is a heat-up procedure that has the advantages of producing high-quality CIS QDs, to be scalable and less expensive since it is characterized by a low waste of solvents and reagents.[16] Yet, this approach generates alkyl-thiol passivated CIS QDs that do not adsorb properly onto TiO_2 electrodes. Therefore, so-formed CIS QDs were tethered onto the electrode by means of elevated voltages.[16,21] Alternatively, ligand exchange with a carboxylic acid like mercaptopropionic acid was proposed, but with scarce yields due to the strong interaction between the quantum dot surface and the native alkyl thiol ligand.[10,22]

Here we propose an approach characterized by a high yield and mild conditions to produce CIS QDs-based photoanodes. In particular, ligand exchange at 70 °C with dihydrolipoic acid (DHLA) allowed us to obtain nanoparticles that strongly bind to a titanium dioxide electrode even at 4 °C. The presence of a CdS layer deposited via SILAR enables high current densities (up to 6.5 mA cm^{-2}).

2. Results and Discussion

2.1. Synthesis and Characterization of CIS QDs

In order to investigate the size effect on the generated photocurrent, two batches of $CuInS_2$ quantum dots with different dimensions were synthesized. The reactions were conducted in the presence of an excess of 1-octanethiol that acts, at the same time, as a solvent, sulfide source, and capping agent. This strategy ensures a total consumption of the metal precursors, lowering the waste, as proved by atomic emission spectroscopy (Table S1, Supporting Information). The size of the octanethiol-capped nanoparticles was estimated by the maximum emission wavelength, as reported in literature (see Supporting Information for details),[24] obtaining 3.4 and 4.1 nm as average diameters of the two samples, respectively (**Figure 1**). Powder X-ray diffraction (XRD) provided insights into the crystallite size (**Figure 2**): 1.9 and 2.7 nm were estimated by Scherrer equation. These results show that a certain amount of amorphous phase is present in the quantum dots lattice. XRD spectroscopy confirms the chalcopyrite phase of the $CuInS_2$, as reported in the literature.[18,24,25] For the smaller-sized QDs (red line) a further peak at 35° is visible and can be attributed to the presence of various chalcopyrite and zinc-blend phases.[26]

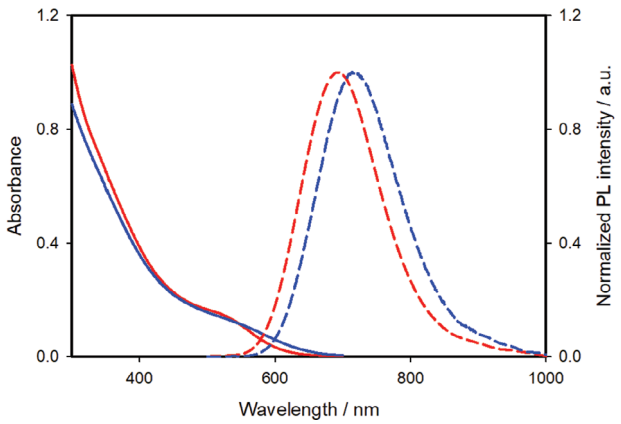

Figure 1. Absorption (solid lines) and emission (dashed lines, excitation at 450 nm) of CIS_{3nm}-OT (red lines) and CIS_{4nm}-OT (blue lines) in air-equilibrated toluene.

© 2024 The Author(s). Advanced Optical Materials published by Wiley-VCH GmbH

21951071, 2024, 19, Downloaded from https://onlinelibrary.wiley.com/doi/10.1002/adom.202400259 by Area Sistemi Dipart & Doc, Wiley Online Library on [24/01/2025]. See the Terms and Conditions (https://onlinelibrary.wiley.com/terms-and-conditions) on Wiley Online Library for rules of use; OA articles are governed by the applicable Creative Commons License

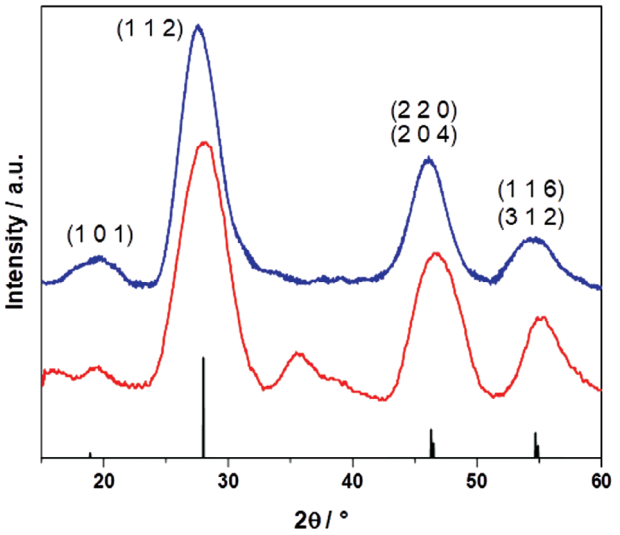

Figure 2. XRD pattern of CIS_{3nm}-OT (red line) and CIS_{4nm}-OT (blue line) and related Miller indexes, compared to the XRD pattern for bulk chalcopyrite (black line).

For simplicity, hereafter we will refer to the two 1-octanethiol capped nanocrystals as CIS_{3nm}-OT for the smaller size and CIS_{4nm}-OT for the bigger size.

Alkyl-capped CIS QDs are known not to adsorb properly onto TiO_2 electrodes and a carboxylic anchoring group is usually employed for the adsorption. However, mercaptocarboxylic acids containing only one thiol group do not replace effectively the native alkyl thiol. The issue can be overcome by performing a ligand exchange with dihydrolipoic acid, which contains two thiol anchoring groups.[5,6,25,27] The presence of polar moieties on the surface of the quantum dots after ligand exchange leads to improved stability of the nanoparticles in polar solvents like methanol or ethanol.

The effectiveness of the ligand exchange was proved by comparing the ^{1}H-NMR spectra in deuterated dimethylsulfoxide (DMSO) of the CIS-DHLA QDs, lipoic acid, and DHLA (Supporting Information). The spectrum of CIS-DHLA QDs displays broad signals at similar chemical shifts with respect to DHLA. The broadening of the peaks has been associated with a hindered motion of the molecules attached to the surface of the quantum dot, yielding a decrease in T_2 relaxation.[28] This effect has been previously noticed by us also for other quantum dots.[25,29,30] The presence of signals related to lipoic acid confirms the instability of the ligand-quantum dot bond in the presence of ambient conditions of temperature and oxygen. It is worth noting that the signals related to hydrogens linked to the sulfur atoms at ≈2.3 ppm disappear when the ligand is attached to the nanoparticle. The absence of the peaks related to the native 1-octanethiol ligand are symptom of a complete replacement with the DHLA moieties.

The most important photophysical data are presented in **Table 2** and Figure 1. In general, 3 nm-sized nanocrystals show lower photoluminescence quantum yield (PLQY) and average lifetime (‹τ›), most likely due to the increased surface-to-volume ratio, which increases the contribution of surface trap states. The difference in emission maxima, emission quantum yield, and emission lifetimes of CIS-DHLA with respect to CIS-OT can be mainly ascribed to the change of polarity of the solvent employed, as occurred for CIS_{4nm}-DHLA dispersed in toluene (Figure S1, Supporting Information), and for the introduction of additional surface defects upon ligand exchange, as reported previously in other examples of ligand exchange reactions.[25,31] The bandgap values of CIS samples were obtained by the Tauc plot obtained from absorption spectra in solution by using the exponent 2 for the direct optical transition (Figure S2a, Supporting Information)[32] CIS_{3nm}-DHLA and CIS_{4nm}-DHLA show a bandgap of 2.13 and 2.03 eV, respectively. Unsurprisingly, the bandgap is not significantly affected by the ligand exchange procedure, as the latter should not affect the inorganic core.

The same bandgap values were obtained from absorption spectra on CIS QDs deposited on TiO_2 thin films, resulting in 2.13 and 2.03 eV for the 3 and 4 nm samples respectively (Figures S2b and S4, Supporting Information), showing that the deposition process does not affect the bandgap of the QDs.

We also estimated the band-gap energy via cyclic voltammetry (CV) measurements of CIS-DHLA deposited on the ZrO_2 electrode (Figure S3, Supporting Information). ZrO_2 was used as an electrochemically inert porous scaffold to enhance the surface loading of quantum dots on the electrode. The CV is characterized by irreversible processes, with a cathodic pre-wave at ≈ −1.2 V versus SCE and anodic wave at ≈0.8 V, affording electrochemical gap values of the order of 2 eV for both the CIS_{3nm}-DHLA and CIS_{4nm}-DHLA, in good agreement with the optical gap extracted from the Tauc analysis. Clearly, the irreversible nature of the voltammetric waves does not allow to appreciate the subtle differences (of the order of ≈ 0.1 eV) in the optical properties of 3 and 4 nm sized quantum dots, but allows to evaluate the energetics of the lowest and highest unoccupied and occupied states respectively, indicating that the charge-separated state eventually induced in these materials can be configured as a relatively good oxidant and an even better reductant.

2.2. Photoelectrochemical Measurements

The deposition of CIS-DHLA onto the FTO-TiO_2 electrode was carried out by simply immersing the electrodes in an alcoholic suspension of the nanoparticles, yielding CIS_{3nm}/TiO_2 and CIS_{4nm}/TiO_2 photoanodes. The adsorption was followed by monitoring the absorption spectrum of the quantum dots on the electrodes, and successful deposition was confirmed by SEM and EDS mapping of the mesoporous thin film cross-section. (Figures S5 and S6, Supporting Information, respectively).

Table 2. Photophysical properties of CIS QDs of different sizes (3 or 4 nm) with a different capping ligand.

	Solvent	Bandgap/eV	λ_{em}/nm	PLQY/%	‹τ›/ns[a)]
CIS_{3nm}-OT	Toluene	2.13	695	0.77	74
CIS_{4nm}–OT	Toluene	2.06	720	7.7	240
CIS_{3nm}-DHLA	EtOH	2.13	705	< 0.1	3
CIS_{4nm}-DHLA	EtOH	2.03	750	1.0	88

[a)] ‹τ› are computed as a weighted average of the lifetimes based on their pre-exponential factors due to a poly-exponential decay of the emission intensity.

© 2024 The Author(s). Advanced Optical Materials published by Wiley-VCH GmbH

21951071, 2024, 19, Downloaded from https://onlinelibrary.wiley.com/doi/10.1002/adom.202400259 by Area Sistemi Dipart & Doc, Wiley Online Library on [24/01/2025]. See the Terms and Conditions (https://onlinelibrary.wiley.com/terms-and-conditions) on Wiley Online Library for rules of use; OA articles are governed by the applicable Creative Commons License

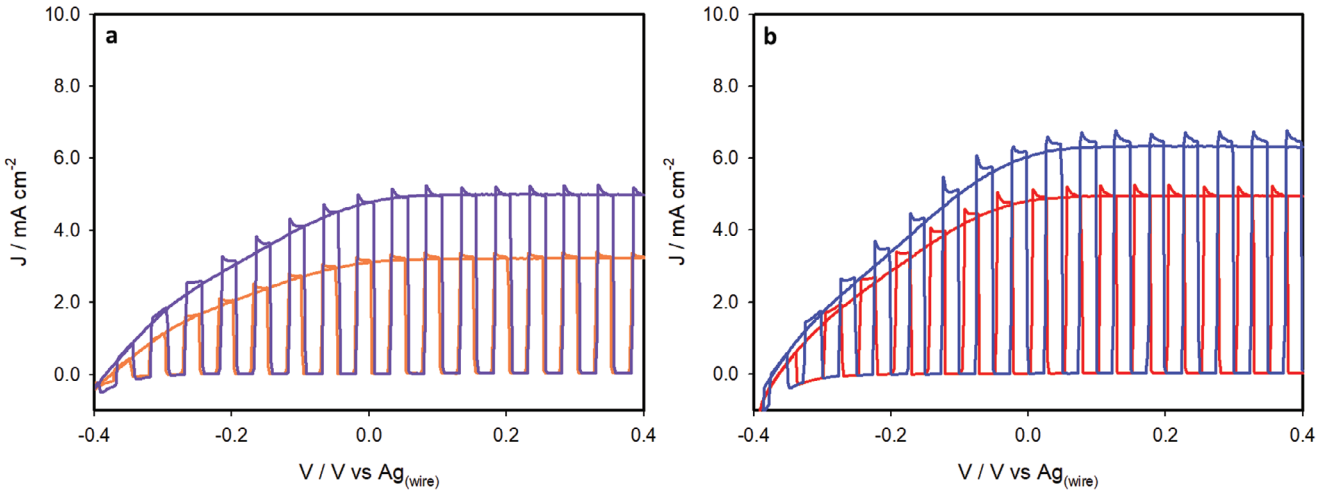

Figure 3. Linear and chopped J/V curves of a) CIS_{3nm} /CdS/TiO_2 and b) CIS_{4nm}/CdS/TiO_2 photoanodes between −0.4 and +0.4 V versus Ag QRE in 1.0 M aqueous Na_2S in the presence (orange and red lines) or absence (violet and blue line) of a 455 nm cutoff filter, under 1-sun equivalent irradiation.

J/V experiments were performed on the CIS/TiO_2 photoanodes under simulated solar irradiation in the presence or absence of a 455 nm cutoff filter and 1.0 M Na_2S as a sacrificial electrolyte. The cutoff filter was used to prevent light absorption by the TiO_2 layer and to avoid the direct water oxidation caused by the holes in TiO_2 valence band and the consequent production of hydroxyl radicals.[33] J/V cycles between −0.3 and +0.4 V versus Ag QRE yielded an increase in the photocurrent for both the CIS_{3nm}/TiO_2 and CIS_{4nm}/TiO_2, reaching a plateau value after ≈50 J/V cycles (Figure S10, Supporting Information). The maximum photocurrent detected was ≈0.8 and 1.6 mA cm^{-2} for CIS_{3nm}/TiO_2 and CIS_{4nm}/TiO_2, respectively, both with or without the 455 nm filter (Figure S11, Supporting Information).

The enhancement in the limit photocurrent was accompanied by a decrease in the absorption spectrum of the photoactive layer (Figure S13, Supporting Information), suggesting that poorly attached CIS QDs are removed by the J/V cycles in the photoelectrochemical cell. In addition to that, a shift of the excitonic peak is observed after the J/V cycles. This phenomenon may be ascribed to a partial corrosion of the inorganic core, which lowers the dimension of the nanocrystals attached to the surface of the electrode and therefore changes their photophysical properties, even if the effect is not appreciable from SEM analyses (Figure S7, Supporting Information).

In order to ameliorate the photocurrent, successive ionic layer adsorption and reaction (SILAR) of CdS was performed, yielding CIS/CdS/TiO_2 photoanodes. The presence of cadmium on the electrodes was proved by energy dispersive X-ray (EDX) analyses (Table S2 and Figure S8, Supporting Information), and the change in surface morphology (Figures S5c and S9, Supporting Information), confirmed the deposition of additional layers. It was found that after eight depositions, the photocurrent reached the maximum value (Figure S12, Supporting Information).

According to the absorption spectra (Figure S13, Supporting Information), the absorption is enhanced either upon the addition of eight layers of CdS or using bigger nanocrystals, which are known to display a higher molar absorption coefficient together with a redshift.[32]

J/V experiments were replicated in the same conditions. For CIS_{3nm}/CdS/TiO_2 photoanodes, the photocurrent reached values as high as 3.0 and 5.0 mA cm^{-2} in the presence or absence of 455 nm cutoff filters, while for CIS_{4nm}/CdS/TiO_2photoanodes, densities of currents up to 5.0 and 6.5 mA cm^{-2} were obtained (**Figure 3**).

Unlike the CIS/TiO_2 photoanodes, no significant change in both the photocurrent and absorption spectrum after several J/V cycles under irradiation was displayed for CIS/CdS/TiO_2, demonstrating a prolonged stability of the photoelectrodes.

The same experiments were performed on bare TiO_2 electrodes upon 8 SILAR deposition of CdS, showing a scarce absorption (Figure S14, Supporting Information) and lower photocurrents if compared to the system comprising the quantum dots.

To gain a deeper understanding of the role of the CdS layers, whether it acted as an independent photoactive material, or, as reported elsewhere,[18] as a shell diminishing the charge recombination pathways, IPCE was performed on both CIS/TiO_2 and CIS/CdS/TiO_2 photoanodes (**Figure 4**).

For the 3 nm quantum dots (Figure 4a), IPCE of CIS_{3nm}/TiO_2 photoanodes reached a maximum of 11% at 440 nm. At the same wavelength, CIS_{3nm}/CdS/TiO_2 reached the highest value of 45%, a fourfold increase if compared to the pristine sensitized electrode. For the CIS_{4nm}/TiO_2 (Figure 4b), the maximum value enhances from 15% to 50% upon CdS deposition, a 3.3-fold increase. The redshift and enhancement of the IPCE for the 4 nm-sized sample is consistent with their absorption profile. At lower wavelengths, a second maximum occurring at 350 nm is attributed to the direct excitation of TiO_2. The enhancement in the IPCE of the CdS-coated electrodes is not limited to the spectral range where CdS layers absorb light (<500 nm, Figure S13, Supporting Information). This is clearly demonstrated by the APCE plots, in which the IPCE plots were divided by the absorbance (Figure 4, hollow points). This observation indicates that the enhancement of photocurrent observed upon CdS deposition is not merely due to the direct absorption of CdS, but rather to its ability to accelerate exciton separation, as depicted in **Figure 5**.

© 2024 The Author(s). Advanced Optical Materials published by Wiley-VCH GmbH

21951071, 2024, 19, Downloaded from https://onlinelibrary.wiley.com/doi/10.1002/adom.202400259 by Area Sistemi Dipart & Doc, Wiley Online Library on [24/01/2025]. See the Terms and Conditions (https://onlinelibrary.wiley.com/terms-and-conditions) on Wiley Online Library for rules of use; OA articles are governed by the applicable Creative Commons License

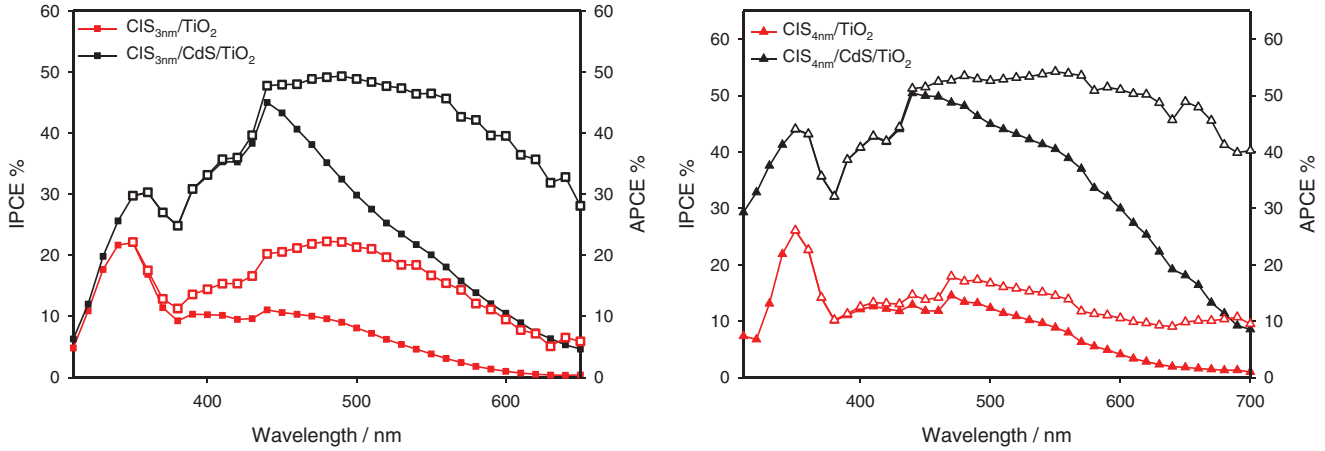

Figure 4. IPCE (0.2 V vs Ag QRE, solid points) and APCE (0.2 V vs Ag QRE, empty points) in the percentage of a) CIS_{3nm}/TiO_2 (red squares) and $CdS/CIS_{3nm}/TiO_2$ (black squares) and b) CIS_{4nm}/TiO_2 (red diamonds) and $CdS/CIS_{4nm}/TiO_2$ photoanodes (black diamonds).

Tauc plots built on IPCE data of CIS/TiO_2 and $CIS/CdS/TiO_2$ substrates afford bandgap values well in agreement with the Tauc plot derived by the absorption of the same specimens, discussed in the previous section. This finding further confirms that the measured optical energy gap is correlated with the photocurrent generation in CIS-sensitized devices.

2.3. Time-Resolved Absorption and Emission Measurements

A better understanding of the charge separation dynamics could be achieved via time-resolved photophysical measurements.

The behavior of CIS-DHLA deposited onto TiO_2 and ZrO_2 (CIS/TiO_2 and CIS/ZrO_2, respectively) was investigated by time-correlated single photon counting technique. Whereas the energies of CIS-DHLA and TiO_2 conduction bands allow the electron transfer from the former to the latter semiconductor, this is not the case for ZrO_2, therefore the comparison of these measurements enables us to evaluate the charge injection dynamics from CIS-DHLA to TiO_2. In the following, only photoanodes based on 4 nm sized CIS-DHLA will be discussed, but similar results were obtained for the 3 nm sized sample (Figures S17 and S19, Supporting Information).

CIS_{4nm}/ZrO_2 shows an emission decay which is well fitted by a biexponential function with amplitude weighted $\langle\tau\rangle$ = 15.3 ns (Figure S18, Supporting Information). The lifetime of CIS-QDs deposited on the ZrO_2 surface is shorter than the lifetime recorded in solution, as expected by surface quenching experienced by the QDs on the electrode surface. Upon deposition of CdS, yielding $CIS_{4nm}/CdS/ZrO_2$, the average lifetime decreases to $\langle\tau\rangle$ = 13.8 ns. This effect agrees with the hypothesis of a charge transfer from CIS-DHLA to CdS, which adds an additional deactivation pathway for CIS-DHLA excitons and therefore shortens their lifetime. Analogous behavior was observed for the 3 nm particles after SILAR deposition of CdS.

The average lifetime of CIS_{4nm}/TiO_2 is lower than that recorded for CIS_{4nm}/ZrO_2 ($\langle\tau\rangle$ = 3.8 ns, Figure S18, Supporting Information), most likely due to charge transfer from CIS-DHLA to TiO_2. Upon CdS deposition, the emission is almost completely quenched, and its decay largely falls within the excitation pulse, yielding an average lifetime of $\langle\tau\rangle$ = 0.58 ns. This effect proves

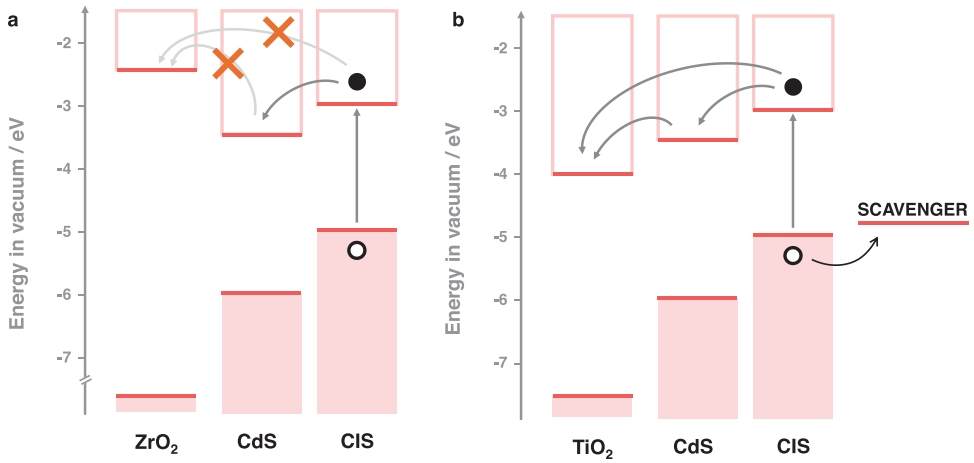

Figure 5. Schematic depiction of the charge transfer dynamics in a) $CIS/CdS/ZrO_2$ and b) $CIS/CdS/TiO_2$. Band energies of TiO_2, ZrO_2, and CdS were taken as those of the bulk materials from Refs.[43,44] CIS band energies were calculated on the basis of cyclic voltammetry measurements.

© 2024 The Author(s). Advanced Optical Materials published by Wiley-VCH GmbH

21951071, 2024, 19, Downloaded from https://onlinelibrary.wiley.com/doi/10.1002/adom.202400259 by Area Sistemi Dipart & Doc, Wiley Online Library on [24/01/2025]. See the Terms and Conditions (https://onlinelibrary.wiley.com/terms-and-conditions) on Wiley Online Library for rules of use; OA articles are governed by the applicable Creative Commons License

that CIS-DHLA can transfer electrons to TiO_2 even in the absence of CdS, but the latter adds further deactivation pathways, diminishing radiative charge recombination (Figure 5). This facilitates charge separation following irradiation, which eventually results in a greater quantity of excitons that are converted to current, raising the device's IPCE as seen in Figure 4.

Transient absorption spectra (TAS) of CIS/TiO_2 were measured in NaOH (0.01 M) and Na_2S (1 M) aqueous solution before and after CdS deposition.

In NaOH solution, TAS of CIS_{4nm}/TiO_2 shows a ground state bleaching (GSB) between 400 and 600 nm (**Figure 6a**), within the instrumental response time (FWHM ≈300 ns). The band centered at 700 nm is associated to the emission of CIS (EM) in competition with the charge injection into TiO_2. At long delay times, the ground state bleaching develops into a broad and featureless band which reaches its maximum intensity after ≈700 ns from the initial excitation. We believe that this band is ascribed to the absorption of CIS_{4nm}/TiO_2 charge separated state (CSS), as the absorption at lower wavelength ($\lambda < 600$ nm) can be associated to the holes in the valence band of CIS (h^+) while the one occurring at higher wavelength ($\lambda > 600$ nm) is attributed to the electrons localized in the conduction band of TiO_2 (e^-).[34,35] Therefore, complete recovery to the QD ground state is not observed within the explored time frame, in agreement with the presence of a kinetic component of slow electronic recombination, often observed at sensitized TiO_2 interfaces.[36] The weak intensity of the signal associated with CIS_{4nm}/TiO_2 charge-separated state is assigned to a non-quantitative transfer from the QDs to the TiO_2 (as a matter of fact, only 10–15% of CIS QDs can inject according to IPCE spectra). Furthermore, it is reasonable to assume that the difference in the molar absorption coefficient of CIS QDs and ground state and the separated charge state is very low, which gives a further explanation for the weakness of the long-lived signal.

In a solution of Na_2S, the same ground state bleaching is observed, while CIS emission is strongly quenched (Figure 6b, negative band centered at 700 nm). This arises from the oxidation of sulfide ions by the excited states of CIS, which competes with their emission. Furthermore, more effective electron injection into TiO_2 is expected as a consequence of the negative shift of CIS flat band potential, determined by sulfide excess that can act as a potential determining ion. At a long delay time, the band associated with CIS_{4nm}/TiO_2 charge-separated state is still visible, although the hole absorption ($\lambda < 600$ nm) is strongly quenched in the time interval comparable to the instrumental response. This effect can be explained considering the sulfide ions absorbed onto CIS QDs surface, which statically consume the holes localized in the valence band of the QDs. A weak absorption at $\lambda < 450$ nm is visible even in the presence of Na_2S. This can be ascribed to the absorption of deep holes (dh^+), which cannot be regenerated by sulfide scavenging, or to Stark effect.[37,38] The latter can be associated with the variation in the absorption of CIS by the electric field produced by the accumulation of negative charges in the TiO_2 electrode. The presence of CdS in $CIS_{4nm}/CdS/TiO_2$ determines an even stronger quenching of CIS emission at 700 nm (Figure 6c), which is in agreement with a faster charge separation that prevents radiative recombination.

2.4. Electrochemical Impedance Spectroscopy

The photoelectrochemical response of the CIS/TiO_2 sensitized electrodes was further investigated by EIS under illumination, in order to gain additional information about the role of CdS in improving the performances of CIS. The impedance response of CIS_{4nm}/TiO_2 was compared to $CIS_{4nm}/CdS/TiO_2$ in the presence of 1 M Na_2S as a sacrificial agent (**Figure 7**). In all cases, the complex plane plots of the photoelectrodes are dominated by a depressed arc exhibiting a projection on the real axis in the range of 100–300 Ω for $CIS_{4nm}/CdS/TiO_2$ and 800–200 Ω for CIS_{4nm}/TiO_2 (Figures S21 and S22, Supporting Information). The real component of the arc was voltage-dependent and well correlated with the J/V curve of the electrodes, as can be appreciated from the R versus $\frac{\partial V}{\partial i}$ plots (Figures S21 and S22, Supporting Information), indicating that indeed we are observing an active element in the photocurrent generation mechanism. This large arc is accompanied by a small high-frequency arc (barely observable in the full scale of the complex plane plots) which however was substantially potentially independent and ascribed to a passive interface (FTO/TiO_2 interface). Thus, in the fitting, we only considered the large potential dependent arc. In the case of CIS_{4nm}/TiO_2, fitting was achieved with a simple Randles circuit comprising a parallel RC mesh, whereas in $CIS_{4nm}/CdS/TiO_2$ a nested RC mesh was used, in order to describe the resistance and capacitance of the CdS layer, which in our view, is an active medium in the charge transfer mechanism.

Constant phase elements (CPE) defined according to (Q(CPE) = Y ×(iω)n) were characterized by exponents n of the order of 0.9, allowing to use directly the CPE admittance Y to compute their equivalent capacitance. The employed models described well the JV behavior of the two electrodes as demonstrated by Figures S21 and S22 (Supporting Information). The decreased charge transfer resistance in the $CIS_{4nm}/CdS/TiO_2$ is associated with a large increase (up to a 10 x factor) in its chemical capacitance, an unambiguous sign of improved charge separation efficiency when CdS is present. The exponential dependence of the capacitance has been reported and predicted many times in nanocrystalline TiO_2-based electrodes, characterized by a density of states N tailing below the conduction band edge according to $N \approx e^{\frac{-\alpha eV}{KT}}$ where α is a tailing parameter and V is the applied voltage.[39] Finally, the time constant $\tau = RC$ provides for both electrodes a similar result (from ≈3 to 0.2 s) within the whole explored voltage range. We noted that R and C for the $CIS_{4nm}/CdS/TiO_2$ account for the total resistance and capacitance of the electrode. The decreased time constant with increasing reverse polarization is consistent with the depletion of charge density due to enhanced charge extraction at the back contact occurring when approaching the *pleateau* value of the JV curves. Thus, τ follows the same trend dictated by the chemical capacitance versus voltage (Figures S23 and S24, Supporting Information). Often, the charge transfer time constant of these semiconductor photoelectrodes has been physically related to the electron lifetime in the semiconductor,[40] proving, that in our case CdS acts primarily in enhancing charge separation rather than retarding recombination, consistent with the photophysical results previously discussed.

© 2024 The Author(s). Advanced Optical Materials published by Wiley-VCH GmbH

21951071, 2024, 19, Downloaded from https://onlinelibrary.wiley.com/doi/10.1002/adom.202400259 by Area Sistemi Dipart & Doc, Wiley Online Library on [24/01/2025]. See the Terms and Conditions (https://onlinelibrary.wiley.com/terms-and-conditions) on Wiley Online Library for rules of use; OA articles are governed by the applicable Creative Commons License

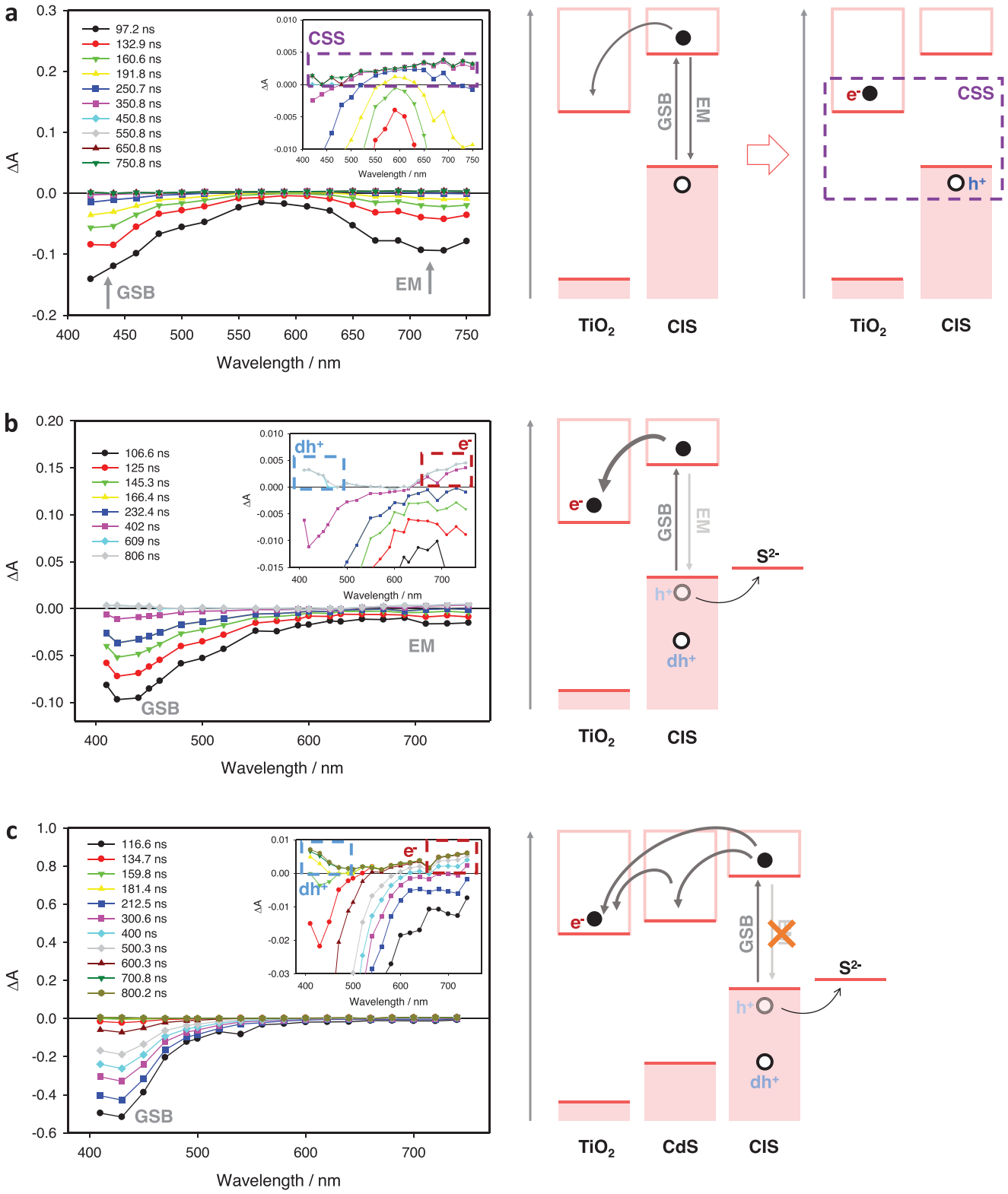

Figure 6. Transient absorption spectroscopy of a) CIS_{4nm}/TiO_2 in 0.01 M NaOH aqueous solution; b) CIS_{4nm}/TiO_2 in 1 M Na_2S aqueous solution and c) $CIS_{4nm}/CdS/TiO_2$ in 1 M Na_2S aqueous solution. A schematic overview of the processes involved is provided. For the sake of clarity, absorption and emission are depicted as band-edge phenomena, neglecting the role of intra-gap states.

© 2024 The Author(s). Advanced Optical Materials published by Wiley-VCH GmbH

21951071, 2024, 19, Downloaded from https://onlinelibrary.wiley.com/doi/10.1002/adom.202400259 by Area Sistemi Dipart & Doc, Wiley Online Library on [24/01/2025]. See the Terms and Conditions (https://onlinelibrary.wiley.com/terms-and-conditions) on Wiley Online Library for rules of use; OA articles are governed by the applicable Creative Commons License

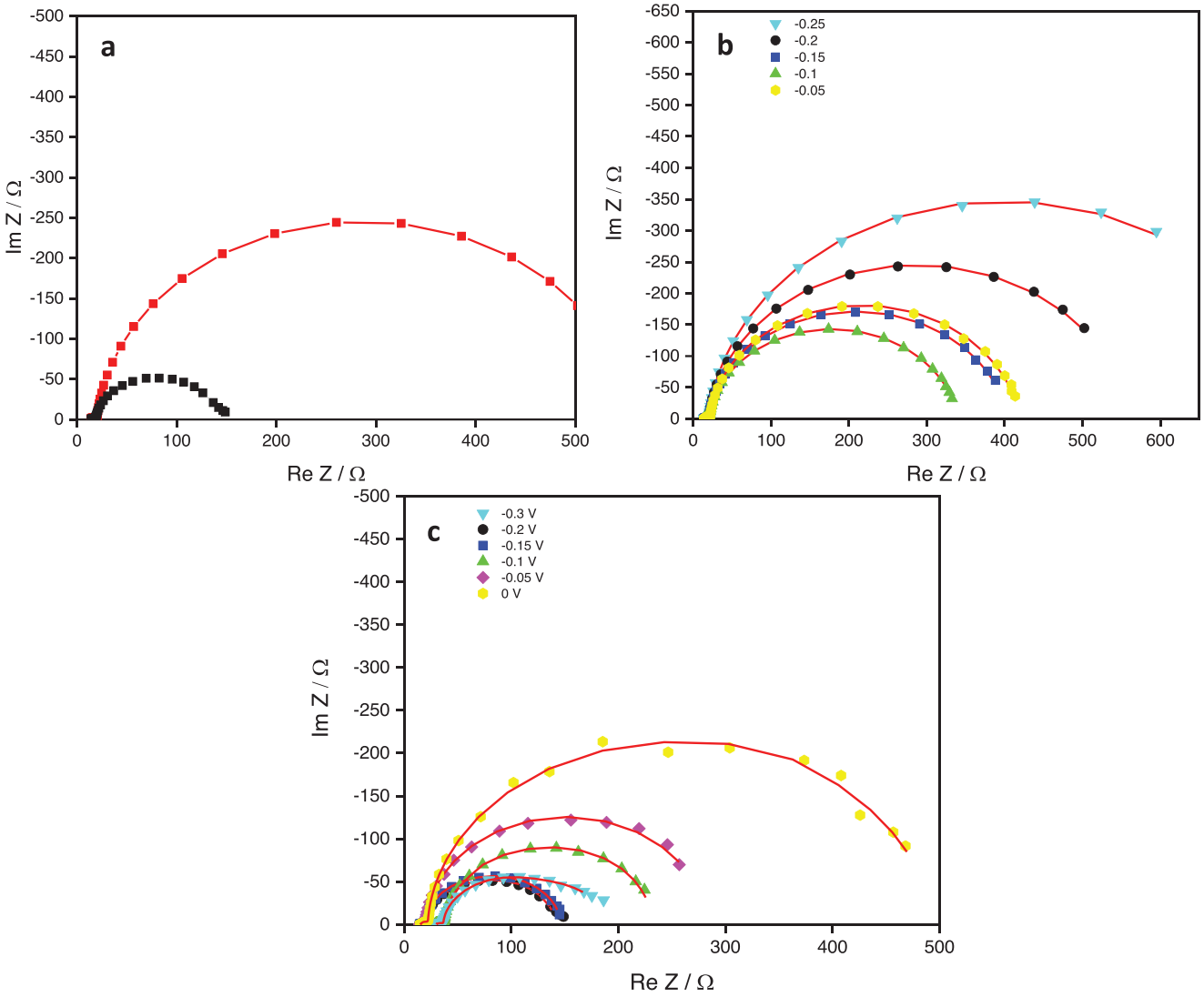

Figure 7. a) Comparison between EIS Nyquist plots of CIS_{4nm}/TiO_2 (black line) and $CIS_{4nm}/CdS/TiO_2$ at −0.2 V (red line); b) CIS_{4nm}/TiO_2 Nyquist plots from −0.25 to −0.05 V; c) $CIS_{4nm}/CdS/TiO_2$ Nyquist plots from −0.3 to 0 V. All measurements are in 1.0 M Na_2S in the presence of a 455-nm cutoff filter under 1-sun irradiation.

3. Conclusion

Two batches of CIS QDs featuring a size of 3 and 4 nm were synthesized via a heat-up procedure which yields high-quality nanoparticles, with low waste of reagents and easy scalability, all important characteristics in view of productions at an industrial level. The quantum dots were successfully tethered onto TiO_2 electrodes with an efficient and safe approach based on i) ligand exchange with DHLA, a molecule obtained by reduction of the widely commercially available lipoic acid, and ii) spontaneous adsorption. The so-obtained photoanodes were tested under solar simulated irradiation in the presence of a Na_2S and displayed a size-dependent photoelectrochemical behavior. Their properties were ameliorated by coating a CdS shell, which improved the efficiency of charge transfer. Interfacial dynamics of the system were investigated by means of solid-state transient spectroscopy. In the best conditions so far identified, maximum IPCEs of the order of 50% and a spectral sensitization extended up to 700 nm were observed. Further studies on reversible redox mediators for the photo-oxidation of water and organic molecules are being pursued in our laboratories.

4. Experimental Section

Materials and Methods: CuI (99.998%), $(AcO)_3In$ (99.99%), 1-octanethiol (97%), 1-octadecene (90%), $Na_2S{\bullet}9H_2O$ (98%) were purchased from Fisher Scientific; chloroform (ACS), methanol (ACS), $NaBH_4$ (99%), (±)-alpha-lipoic acid, 1-butanol (99.4%) (ACS), titanium isopropoxide, $Cd(NO_3)_2{\bullet}4H_2O$ (98%), $TiCl_4$ (99.99%), and the other reagents were purchased from Sigma–Aldrich and used without further purification. FTO TEC-7 was bought from NSG, and 18NR-T TiO_2 paste was purchased from Solaronix.

The syntheses of the quantum dots were performed by using a J-KEM Scientific Gemini 230 temperature controller with two thermocouples

© 2024 The Author(s). Advanced Optical Materials published by Wiley-VCH GmbH

21951071, 2024, 19, Downloaded from https://onlinelibrary.wiley.com/doi/10.1002/adom.202400259 by Area Sistemi Dipart & Doc, Wiley Online Library on [24/01/2025]. See the Terms and Conditions (https://onlinelibrary.wiley.com/terms-and-conditions) on Wiley Online Library for rules of use; OA articles are governed by the applicable Creative Commons License

(uncoated K probes with a diameter of 1/8 inches) connected to 100 mL soft shell heating mantles.

Nuclear magnetic resonance (^{1}H and ^{13}C-NMR) spectra were measured on an ARX Varian INOVA 400 (400 MHz) spectrometer in deuterated solvents; chemical shifts are reported in parts per million (ppm) and the multiplicity as follows: s = singlet, d = doublet, t = triplet, q = quartet, b = broad, m = multiplet.

LC-electrospray ionization mass spectra were obtained with an Agilent Technologies MSD1260 Infinity with a single-quadrupole mass spectrometer and an isocratic elution with a mixture of water and acetonitrile as the eluent phase.

Size exclusion chromatography (SEC) was performed over Sephadex LH-20 Support using methanol as an eluent solvent.

The elemental composition of CIS QDs was determined via an Agilent 4210 MP-AES atomic emission spectrometer. To this purpose, 0.2 mL of the purified octanethiol-passivated CIS QDs (average size, 4 nm) was digested into 3 mL of 7 M nitric acid.

Powder XRD measurements were performed on a Panalytical X'Pert Pro powder diffractometer equipped with a Cu X-ray tube (Kα radiation, 1.54184 Å, 40 mA, 40 kV), with a Bragg–Brentano configuration and X'celerator detector. Typically, a 0.5 micromolar suspension of CIS QDs in chloroform was precipitated in MeOH, desiccated at a rotary evaporator and a rotative pump, and deposited onto a zero-background silicon sample holder. A continuous scan from 10° to 90° was performed with an acquisition time of 50 min.

Field Emission – Scanning Electron Microscopy was performed on Zeiss LEO 1530 FE-SEM equipped with X-act – 10 mm^2 SDD EDS Detector by Oxford Instruments. Micrographs were collected operating at V_{acc} = 5 keV.

Photophysical measurements were carried out in air-equilibrated HPLC chloroform, toluene, or ethanol at 298 K or deposited on TiO_2-FTO electrodes. UV–vis absorption spectra were recorded with a Perkin Elmer λ650 spectrophotometer, using quartz cells with a 1.0 cm path length. Emission spectra were obtained with either a Perkin Elmer LS-50 spectrofluorometer equipped with a Hamamatsu R928 phototube or an Edinburgh FS5 with a PMT980 and an InGaAs detector for visible and NIR spectral range, respectively. Correction of the emission spectra for detector sensitivity in the 550–1000 nm spectral region was performed by a calibrated lamp.[41] Emission quantum yields were measured following the method of Demas and Crosby[42] (the standard used: $[Ru(bpy)_3]^{2+}$ in air-equilibrated aqueous solution Φ = 0.0407). PL lifetime measurements of solutions of CIS QDs in the range 0.5 ns–1 µs were performed by an Edinburgh FLS920 spectrofluorometer equipped with a TCC900 card for data acquisition in time-correlated single photon counting experiments (0.2 ns time resolution) with a 340 nm-pulsed diode and an LDH-P-C-405 pulsed diode laser. The estimated experimental errors are 2 nm on the band maxima, 5% on the luminescence lifetime, and 10% on the emission quantum yield.

Emission lifetimes of the CIS QDs deposited on solid substrates (TiO_2, ZrO_2) were acquired with a Picoquant Picoharp 300 time-correlated single photon counting by using a 480 nm pulsed LED source. Levenberg-Marquardt fitting/deconvolution of the decay histogram was accomplished with a bi-exponential function by the dedicated Fluofit program. In general, fits satisfied the statistical acceptability criteria, with $\chi^2 \approx 1$ and residuals R(i) = W(i)(Decay(i)-Fit(i)) < 4 standard deviations fluctuating around 0 within all the fitting intervals. Here, W(i) = 1/(Decay(i))$^{1/2}$ defines the intensity weight in a given channel (i) according to the Poisson distribution while Decay(i) and Fit(i) are the experimentally measured and calculated decay values, respectively

Transient Absorption Spectroscopy (TAS) was accomplished with a custom-built apparatus described in recent publications.[43] Excitation was at 355 nm and, in the presence of a 350 Ω amplifying input impedance, the instrumental time response of the spectrometer was of the order of 300 ns. Excitation energy was at 15 mJ cm^{-2}/pulse, at a frequency of 0.2 Hz (the laser excitation frequency was limited by the synchronized pulsing of the probe beam). Experiments were carried out on the photoanodes under open circuit conditions (disconnected wires).

Photoelectrochemical measurements were carried out with a Metrohm Autolab PGSTAT 302/N electrochemical workstation (Methrom Autolab, Utrecht, The Netherlands) under solar simulated illumination with an ABET Sun Simulator (ABET Technologies, Milford, CT, USA) equipped with AM 1.5G filter. The incident irradiance was set to 0.1 W cm^{-2} with a Newport Power Meter model 1918-c equipped with a Thermopile (818P-015-18). Pulsed illumination experiments were obtained with a Thorlabs electronic shutter with a frequency of 0.4 Hz. All photoelectrochemical experiments were carried out in a three-electrode cell by using aqueous 1 M Na_2S as an electrolyte, a silver wire as a quasi-reference electrode, a platinum wire as a counter electrode, and the QDs-deposited onto TiO_2-FTO were used as the working electrodes. J/V (Current Density vs Voltage) curves of the photoelectrodes were recorded by multiple scanning analyses in a range of voltage between −0.45 and 0.4 V versus Ag QRE at a scan rate of 20 mV s^{-1}, while chronoamperometries were performed at 0.1 V versus Ag QRE (Figure S16, Supporting Information).

Photoaction spectra (IPCE = Incident Photon to electron Conversion Efficiency) were collected in a three-electrode cell, under mono-chromatic illumination generated by the coupling of a Luxtel 175 W Xe lamp to an applied photophysics monochromator (Luxtel, Danvers, MA, USA), using a spectral bandwidth of 10 nm and a constant potential of 0.2 V versus Ag QRE using the same three electrodes and potentiostat described for J/V experiments. Incident irradiance was measured with a calibrated silicon photodiode while the short circuit photocurrents were measured with an Agilent 34 401 A multimeter.

Electrochemical impedance spectroscopy (EIS) on the CIS-sensitized TiO_2 electrodes was carried out under AM 1.5 illumination in 1 M Na_2S in the presence of a 455 nm cut-off filter. A sinusoidal perturbation voltage having a 10-mV amplitude was applied in the frequency range 30 kHz – 0.01 Hz. Various voltages (vs Ag QRE) were sampled along the descending branch of the JV curve of each electrode. Fitting in terms of equivalent circuits was accomplished by Z view.

Synthesis of CIS QDs: The synthesis of the quantum dots was adapted from strategies reported in the literature.[16,24,25] Copper(I) iodide (48 mg, 0.25 mmol) and indium(III) acetate (73 mg, 0.25 mmol) were suspended in 4 mL of 1-octanethiol and 6 mL of 1-octadecene in a three-necked 100 mL round-bottomed flask equipped with condenser. The suspension was purged twice under two vacuum/nitrogen flux cycles for an hour. The temperature was raised to 120 °C to complete the dissolution of the solids. After 30 min, the flask was heated up to 205 °C, noticing the change in color (from yellow to orange to red to dark red). The suspension was let stir for 30 min (to yield 3 nm-sized octanethiol-capped CIS QDs, referred to as CIS_{3nm}-OT) or 90 min (4 nm-sized octanethiol-capped CIS QDs, referred to as CIS_{4nm}-OT) at 200 °C and then quenched by dipping the flask in a cold-water bath.

The suspension was diluted with chloroform (1:1) and acetone (10:1) was added to make the nanocrystals precipitate. The suspension was centrifuged (two times, 8000 rpm, 10 min each), the supernatant discarded and the precipitate dissolved in chloroform, yielding ≈1.5 µmol of CIS QDs.

Synthesis of Dihydrolipoic Acid (DHLA): One gram of (±)-α-lipoic acid (5 mmol) was dissolved in 20 mL of a 0.25 M aqueous solution of $NaHCO_3$. At 0 °C, 720 mg of $NaBH_4$ (20 mmol) was added in small portions. *Caution!* Sodium borohydride liberates hydrogen gas when in contact with water. The solution color changed immediately from yellow to colorless. The reaction was stirred for 2 h in an ice-water bath and quenched with the addition of HCl 37% until the pH reached ≈1. The solution was extracted three times with toluene. The organic phase was collected and desiccated over Na_2SO_4, and the solvent evaporated yielding dihydrolipoic acid (DHLA) as a colorless oil (yield >99%).

^{1}H-NMR (400 MHz, $CDCl_3$), δ (ppm): 2.95 (m, 1 H, -CH-SH); 2.73 (m, 2 H, -CH_2-SH); 2.42 (t, 2 H, —CH_2—C═O); 1.93 (m, 2 H); 1.82–1.47 (m, 6 H); 1.39 (t, 1 H, HS-CH_2); 1.34 (d, 1 H, HS-CH).

^{13}C-NMR (400 MHz, $CDCl_3$), δ (ppm): 180.1; 42.9; 39.4; 38.8; 34.0; 26.6; 24.4; 22.4.

HPLC-MS (ESI). Found (m/z): [M+NH_4^+] = 226.145; [M+Na^+] = 231.045.

© 2024 The Author(s). Advanced Optical Materials published by Wiley-VCH GmbH

21951071, 2024, 19, Downloaded from https://onlinelibrary.wiley.com/doi/10.1002/adom.202400259 by Area Sistemi Dipart & Doc, Wiley Online Library on [24/01/2025]. See the Terms and Conditions (https://onlinelibrary.wiley.com/terms-and-conditions) on Wiley Online Library for rules of use; OA articles are governed by the applicable Creative Commons License

Ligand Exchange: Ligand exchange procedure was performed via a procedure found in literature and adopted in the laboratories.[25,44] A suspension of 1 µmol of CIS-OT in chloroform was precipitated upon the addition of methanol and centrifuged at 8000 rpm for 6 min. The supernatant was discarded and the precipitate was redispersed in 1 mL of chloroform to transfer it in a 25-mL 2-knecked round-bottom flask equipped with a condenser. Methanol (5 mL) was then poured, to make the nanoparticles precipitate. A hundred microliters of dihydrolipoic acid (0.5 mmol) were added. The mixture was refluxed for 5 h and stirred overnight at room temperature, yielding a limpid brownish suspension. After concentrating at the rotary evaporator, 1 mL of ethanol and 100 µL of chloroform were added. The nanoparticles were precipitated upon the addition of 10 mL of toluene and 25 mL of cyclohexane and centrifuged twice (8000 rpm at 10 °C, 6 min each). The two liquid phases that resulted in the centrifuge tube were separated and the one at the bottom containing the dihydrolipoic acid-capped CIS QDs (hereafter referred to as CIS-DHLA) was diluted with methanol.

Size exclusion chromatography in methanol was performed to further purify the sample. The resulting suspension was diluted with ethanol and stored in a refrigerator inside an 8 mL vial at 4 °C.

Preparation of CIS QDs-Based Photoanodes: To improve the adsorption efficiency of CIS-DHLA, TiO_2 was deposited on fluorinated tin oxide (FTO) electrodes, which were previously ultrasonicated in 2-propanol, in a multistep approach: i) for the first layer, a solution of Ti-isopropoxide 0.3 M in 1-butanol was deposited via spin coating in a two step-ramp (1000 rpm for 9 s and 2000 rpm for 20 s) then the layer was heated at 500 °C for 30 min; ii) a second layer of TiO_2 nanoparticles was deposited by doctor blading using a TiO_2 paste (Solaronix 18NR-T), 3 M Scotch tape was used as spacer, the film was dried with hot air and heated at 550 °C for 45 min; iii) a third layer was introduced by soaking the electrode in $TiCl_4$ 0.4 M overnight, then it was washed with distillated water, dried and heated at 550 °C for 45 min. The electrodes were cut to display either a 1 or a 0.7 cm^2 TiO_2 phase.

For the adsorption of CIS-DHLA, the electrodes were immersed in an ethanol suspension of CIS (1 µmol in ≈5 mL) inside a crystallizing dish, covered with Parafilm, and left to adsorb overnight in a refrigerator at 4 °C.

Supporting Information

Supporting Information is available from the Wiley Online Library or from the author.

Acknowledgements

This project has received funding from the European Union's Horizon 2020 research and innovation program under grant agreement No. 101006839 (CONDOR). V.C. acknowledges PON research and Innovation 2014-2020 (art. 24, comma 3, lett. (a), Law n. 240, December 30th, 2010 and s.m.i. and D.M. n. 1062, August 10th, 2021).

Conflict of Interest

The authors declare no conflict of interest.

Data Availability Statement

The data that support the findings of this study are available from the corresponding author upon reasonable request.

Keywords

adsorption, interfacial dynamics, ligand exchange, nanocrystals, nanoparticles, photoelectrodes, SILAR

Received: January 29, 2024
Revised: March 26, 2024
Published online: May 3, 2024

[1] Z. Du, M. Artemyev, J. Wang, J. Tang, *J. Mater. Chem. A* **2019**, *7*, 2464.
[2] S. Rühle, M. Shalom, A. Zaban, *ChemPhysChem* **2010**, *11*, 2290.
[3] X. Tong, Y. Zhou, L. Jin, K. Basu, R. Adhikari, G. S. Selopal, X. Tong, H. Zhao, S. Sun, A. Vomiero, Z. M. Wang, F. Rosei, *Nano Energy* **2017**, *31*, 441.
[4] Z. Pan, H. Rao, I. Mora-Seró, J. Bisquert, X. Zhong, *Chem. Soc. Rev.* **2018**, *47*, 7659.
[5] G. Morselli, M. Villa, A. Fermi, K. Critchley, P. Ceroni, *Nanoscale Horiz.* **2021**, *6*, 676.
[6] J. Kolny-Olesiak, H. Weller, *ACS Appl. Mater. Interfaces* **2013**, *5*, 12221.
[7] H. Zhong, Z. Bai, B. Zou, *J. Phys. Chem. Lett.* **2012**, *3*, 3167.
[8] A. D. P. Leach, J. E. Macdonald, *J. Phys. Chem. Lett.* **2016**, *7*, 572.
[9] S. Higashimoto, M. Murano, T. Arase, S. Mukai, M. Azuma, M. Takahashi, *Sol. Energy Mater. Sol. Cells* **2017**, *169*, 203.
[10] C. C. Chang, J. K. Chen, C. P. Chen, C. H. Yang, J. Y. Chang, *ACS Appl. Mater. Interfaces* **2013**, *5*, 11296.
[11] Z. Pan, I. Mora-Sero, Q. Shen, H. Zhang, Y. Li, K. Zhao, J. Wang, X. Zhong, J. Bisquert, *J. Am. Chem. Soc.* **2014**, *136*, 9203.
[12] A. Raevskaya, O. Rosovik, A. Kozytskiy, O. Stroyuk, V. Dzhagan, D. R. T. Zahn, *RSC Adv.* **2016**, *6*, 100145.
[13] A. S. Fuhr, H. J. Yun, N. S. Makarov, H. Li, H. McDaniel, V. I. Klimov, *ACS Photonics* **2017**, *4*, 2425.
[14] F. Shen, W. Que, Y. Liao, X. Yin, *Ind. Eng. Chem. Res.* **2011**, *50*, 9131.
[15] V. Singh, I. J. C. Beltran, J. C. Ribot, P. Nagpal, *Nano Lett.* **2014**, *14*, 597.
[16] L. Li, A. Pandey, D. J. Werder, B. P. Khanal, J. M. Pietryga, V. I. Klimov, *J. Am. Chem. Soc.* **2011**, *133*, 1176.
[17] T. L. Li, H. Teng, *J. Mater. Chem.* **2010**, *20*, 3656.
[18] C. Wang, X. Tong, W. Wang, J. Y. Xu, L. V. Besteiro, A. I. Channa, F. Lin, J. Wu, Q. Wang, A. O. Govorov, A. Vomiero, Z. M. Wang, *ACS Appl. Mater. Interfaces* **2020**, *12*, 36277.
[19] Z. Peng, Y. Liu, L. Wu, Y. Zhao, K. Chen, W. Chen, *Appl. Surf. Sci.* **2016**, *388*, 437.
[20] M. Han, W. Chen, H. Guo, L. Yu, B. Li, J. Jia, *J. Power Sources* **2016**, *318*, 121.
[21] Y. C. Chen, H. H. Chang, Y. K. Hsu, *ACS Sustainable Chem. Eng.* **2018**, *6*, 10861.
[22] X. Hu, Q. Zhang, X. Huang, D. Li, Y. Luo, Q. Meng, *J. Mater. Chem.* **2011**, *21*, 15903.
[23] R. Wang, X. Tong, A. I. Channa, Q. Zeng, J. Sun, C. Liu, X. Li, J. Xu, F. Lin, G. S. Selopal, F. Rosei, Y. Zhang, J. Wu, H. Zhao, A. Vomiero, X. Sun, Z. M. Wang, *J. Mater. Chem. A* **2020**, *8*, 10736.
[24] M. Booth, A. P. Brown, S. D. Evans, K. Critchley, *Chem. Mater.* **2012**, *24*, 2064.
[25] G. Morselli, A. Gradone, V. Morandi, P. Ceroni, *Nanoscale* **2022**, *14*, 3013.
[26] P. M. Allen, M. G. Bawendi, *J. Am. Chem. Soc.* **2008**, *130*, 9240.
[27] L. Li, T. J. Daou, I. Texier, T. T. K. Chi, N. Q. Liem, P. Reiss, *Chem. Mater.* **2009**, *21*, 2422.
[28] J. De Roo, *Chem. Mater.* **2023**, *35*, 3781.
[29] R. Mazzaro, A. Gradone, S. Angeloni, G. Morselli, P. G. Cozzi, F. Romano, A. Vomiero, P. Ceroni, *ACS Photonics* **2019**, *6*, 2303.
[30] G. Morselli, F. Romano, P. Ceroni, *Faraday Discuss.* **2020**, *222*, 108.
[31] N. Tsolekile, S. Parani, M. C. Matoetoe, *Nano-Struct. Nano-Objects* **2017**, *12*, 46.
[32] A. R. Zanatta, *Sci. Rep.* **2019**, *9*, 11225.

© 2024 The Author(s). Advanced Optical Materials published by Wiley-VCH GmbH

21951071, 2024, 19, Downloaded from https://onlinelibrary.wiley.com/doi/10.1002/adom.202400259 by Area Sistemi Dipart & Doc, Wiley Online Library on [24/01/2025]. See the Terms and Conditions (https://onlinelibrary.wiley.com/terms-and-conditions) on Wiley Online Library for rules of use; OA articles are governed by the applicable Creative Commons License

[33] Y. Nosaka, A. Nosaka, *ACS Energy Lett.* **2016**, *1*, 356.
[34] M. Mazzanti, S. Caramori, M. Fogagnolo, V. Cristino, A. Molinari, *Nanomaterials* **2020**, *10*, 1.
[35] D. Bahnemann, A. Henglein, J. Lilie, L. Spanhel, *J. Phys. Chem.* **1984**, *88*, 709.
[36] B. C. O'Regan, J. R. Durrant, *Acc. Chem. Res.* **2009**, *42*, 1799.
[37] S. Ardo, Y. Sun, A. Staniszewski, F. N. Castellano, G. J. Meyer, *J. Am. Chem. Soc.* **2010**, *132*, 6696.
[38] E. Marchini, M. Darari, L. Lazzarin, R. Boaretto, R. Argazzi, C. A. Bignozzi, P. C. Gros, S. Caramori, *Chem. Commun.* **2020**, *56*, 543.
[39] J. Bisquert, *Phys. Chem. Chem. Phys.* **2003**, *5*, 5360.
[40] J. Bisquert, F. Fabregat-Santiago, in *Dye-Sensitized Solar Cells*, EPFL Press, New York, **2010**.
[41] M. Montalti, A. Credi, L. Prodi, M. T. Gandolfi, in *Handbook of Photochemistry*, 3rd ed., Taylor & Francis, England **2006**.
[42] G. A. Crosby, J. N. Demas, *J. Phys. Chem.* **1971**, *75*, 991.
[43] A. Reddy-Marri, E. Marchini, V. D. Cabanes, R. Argazzi, M. Pastore, S. Caramori, P. C. Gros, *Chem. Sci.* **2023**, *14*, 4288.
[44] H. T. Uyeda, I. L. Medintz, J. K. Jaiswal, S. M. Simon, H. Mattoussi, *J. Am. Chem. Soc.* **2005**, *127*, 3870.

© 2024 The Author(s). Advanced Optical Materials published by Wiley-VCH GmbH

21951071, 2024, 19, Downloaded from https://onlinelibrary.wiley.com/doi/10.1002/adom.202400259 by Area Sistemi Dipart & Doc, Wiley Online Library on [24/01/2025]. See the Terms and Conditions (https://onlinelibrary.wiley.com/terms-and-conditions) on Wiley Online Library for rules of use; OA articles are governed by the applicable Creative Commons License